Astronomy & Astrophysics manuscript no. finalW49B
23rd February 2006

The X-ray emission of the supernova remnant W49B observed with *XMM-Newton*

M. Miceli[1,2,3], A. Decourchelle[1], J. Ballet[1], F. Bocchino[3], J.P. Hughes[4], U. Hwang[5,6], and R. Petre[6]

[1] DSM/DAPNIA/Service d'Astrophysique, AIM-UMR 7158, CEA Saclay, 91191 Gif-sur-Yvette Cedex, France
[2] Dipartimento di Scienze Fisiche ed Astronomiche, Sezione di Astronomia, Università di Palermo, Piazza del Parlamento 1, 90134 Palermo, Italy
[3] INAF - Osservatorio Astronomico di Palermo, Piazza del Parlamento 1, 90134 Palermo, Italy
[4] Department of Physics and Astronomy, Rutgers University, 136 Frelinghuysen Road, Piscataway, NJ 08854-8109, USA
[5] Center for Astrophysical Sciences, The Johns Hopkins University, 3400 Charles St, Baltimore MD 21218.
[6] Laboratory for High Energy Astrophysics, Goddard Space Flight Center, Greenbelt, MD 20771, USA

Received, accepted

Abstract

Context. In the framework of the study of supernova remnants and their complex interaction with the interstellar medium, we report on an *XMM-Newton* EPIC observation of the Galactic supernova remnant W49B.
Aims. We investigate the spatial distribution of the chemical and physical properties of the plasma, so as to get important constraints on the physical scenario, on the dynamics of the supernova explosion, and on the interaction of the supernova remnant with the ambient interstellar clouds.
Methods. We present line images, equivalent width maps, and a spatially resolved spectral analysis of a set of homogeneous regions.
Results. The X-ray spectrum of W49B is characterized by strong K emission lines from Si, S, Ar, Ca and Fe. In all the regions studied, the X-ray spectrum is dominated by the emission from the ejecta and there is no indication of radial stratification of the elements. A high overabundance of Ni ($Ni/Ni_{\odot} = 10^{+2}_{-1}$) is required in the bright central region and the previous detection of Cr and Mn line emission is confirmed. Spectra are well described by two thermal components in collisional ionization equilibrium. We observe spatial variations in the temperature, with the highest temperature found in the east and the lowest in the west.
Conclusions. Our results support a scenario in which the X-ray emission comes from ejecta interacting with a dense belt of ambient material, but another possibility is that the remnant is the result of an asymmetric bipolar explosion with the eastern jet being hotter and more Fe-rich than the western jet. The eastern jet is confined by interaction with ambient molecular clouds. Comparison of the observed abundances with yields for hypernova and supernova nucleosynthesis does not directly support the association of W49B with a γ-ray burst, although it remains possible.

Key words. X-rays: ISM – ISM: supernova remnants – ISM: individual object: W49B

1. Introduction

Supernova remnants (SNRs) are powerful sources of heavy elements and energy in the interstellar medium (ISM). The supernova supersonic material (ejecta) is expelled into the ambient medium and produces a shock front that heats and ionizes the ISM. As this shock expands into the ISM, a reverse shock associated with the deceleration of the ejecta propagates inward (in the reference frame of the expanding ejecta), thus heating the expelled material to X-ray emitting temperatures. The resulting X-ray emission provides important information about the emitting conditions and the chemical composition of the ejecta.

The galactic supernova remnant W49B is one of the brightest ejecta-dominated SNRs observed in X-rays. It has a center-filled morphology in X-rays and a shell-like morphology in the radio band. According to Rho & Petre (1998), W49B is similar to mixed-morphology supernova remnants, but its classification is uncertain. W49B is one of the 10 galactic sources with the highest surface brightness at 1 GHz (Moffett & Reynolds 1994). The diameter of the radio shell is $\sim 4'$ and the distance to the remnant, estimated on the basis of HI absorption (Radhakrishnan et al. 1972), is $\sim$ 8 kpc (considering the corrections by Moffett & Reynolds 1994).

In the X-ray band, W49B was first detected with the *Einstein Observatory* (Pye et al. 1984). The discovery of intense Fe XXV K line emission by *EXOSAT* (Smith et al. 1985) indicated that the X-ray emission of W49B is thermal and dominated by the ejecta. This result has been further confirmed by analysis of the *ASCA* spectrum (Fujimoto et al. 1995, Hwang et al. 2000). Ejecta-dominated remnants are expected to be rel-

Send offprint requests to: M. Miceli,
e-mail: `miceli@astropa.unipa.it`

atively young, and while the age of W49B has not yet been determined accurately, published age estimates are in the range of ∼ 1000 – 4000 yr (Pye et al. 1984, Smith et al. 1985, Hwang et al. 2000). The images of Si, S and Fe K emission lines obtained with *ASCA* indicate that the iron emission is confined to the inner part of the remnant, while silicon and sulfur emission appears to originate from the outer regions. This result has been interpreted as evidence for a stratified distribution of the elements (Fujimoto et al. 1995). The analysis of the same *ASCA* data carried out by Hwang et al. (2000) showed that broadband modeling of the remnant's global spectrum requires two thermal components and significant overabundances of Si, S, Ar, Ca, Fe with respect to the solar values. Recently, the comparison between data obtained in X-rays with the *Chandra* satellite and in the infrared with the Palomar observatory have revealed new details of the morphology of W49B (Keohane et al. 2004). In particular, the presence of an elongated structure in the Fe K emission (interpreted by the authors as a jet), and the nondetection of a neutron star associated with the remnant, have been considered to make W49B consistent with theoretical predictions for a collapsar (e.g., MacFadyen & Woosley 1999) and thus a candidate for a gamma-ray burst remnant.

Here we present the analysis of an *XMM-Newton* EPIC observation of W49B. The high sensitivity of *XMM-Newton* provides deep insights into the spatial distribution of the elements and the physical conditions in the remnant which lead to important constraints on the physical scenario. The paper is organized as follows: Sect. 2 presents the EPIC data and describes the data processing procedure; Sect. 3 presents the X-ray results in terms of the global spectrum (3.1), imaging (3.2) and spatially resolved spectral analysis (3.3). Sect. 4 discusses the results in the context of observations at other wavelengths and SN models. Finally, we draw our conclusions in Sect. 5.

2. Data processing

The *XMM-Newton* data presented here consist of two observations Observation ID 0084100401 and 0084100501 (PI A. Decourchelle) performed on 3 April 2004 and 5 April 2004 with the EPIC MOS (Turner et al. 2001) and EPIC pn (Strüder et al. 2001) cameras, as summarized in Table 1 . Both observations have pointing coordinates α (2000) = $19^h11^m13^s$ and δ (2000) = $9°7'1''$. A third data set 0084100601 (with the same pointing coordinates) is heavily contaminated by proton flares and was not used for our analysis.

The data were processed using the Science Analysis System (SAS V6.1.0). To create light curves, images and spectra, we selected events with PATTERN≤ 12 for the MOS cameras, PATTERN≤ 4 for the pn camera, and FLAG= 0 for both. To eliminate the contamination by soft proton flares, we screened the data by applying a count-rate limit on the light curves at high energies (10 – 12 keV for MOS and 12 – 14 keV for the pn camera). With a δt = 100 s binning for the light curves, we set the count-rate limit at 18 counts per bin for the MOS cameras, and 22 counts per bin for the pn camera. The exposure times are given in Table 1. For each camera we merged

Table 1. Relevant information about the data.

OBS_ID	CAMERA	t_{exp} (ks)*	Mode	Filter
0084100401	MOS1	18.6/15.8	Large Wind.	medium
0084100401	MOS2	18.7/16.0	Large Wind.	medium
0084100401	pn	17.0/12.9	Full Frame	medium
0084100501	MOS1	18.7/16.8	Large Wind.	medium
0084100501	MOS2	18.7/16.3	Large Wind.	medium
0084100501	pn	17.0/14.6	Full Frame	medium

* Unscreened/Screened exposure time.

the screened event files of the two observations using the task *MERGE*.

All the images presented here are superpositions of the MOS1, MOS2 and pn images (obtained using the *EMOSAIC* task) and are background-subtracted, vignetting corrected and adaptively smoothed. Despite being relatively small in extent compared to the *XMM-Newton* field of view, W49B has a high X-ray brightness and contaminates the local background. For this reason, we used the high signal-to-noise background event files E1_fm0000_M1.fits, E1_00fm00_M2.fits, E1_0000fm_PN.fits (obtained using the medium filter) described in detail in Read & Ponman (2003). The exposure and vignetting correction were performed by dividing the superposed count images by the corresponding superposed exposure maps (produced using the task *EEXPMAP*). The pn exposure maps were scaled by the ratio of the pn/MOS effective areas to make MOS-equivalent superposed count rate images. We smoothed the images adaptively to a signal-to-noise ratio of 10 using the task *ASMOOTH*. The background-subtracted count images and the background- and continuum-subtracted line images (Sect. 3.2) were smoothed while accounting for their variances. The resulting template was then applied to smooth the associated exposure maps before performing the image division. The continuum under the lines was estimated by scaling a continuum band adjacent to the line emission using the continuum spectral slope derived from the global remnant spectrum. The energy ranges chosen for the lines and the continua are listed in Table 2. In all the line bands, the background is ≲ 0.5% of the total signal, except for the 7.65 – 8.0 keV band where it is ∼ 3.6% of the total signal. In the continuum band 4.4 – 6.2 keV, the background amounts to ∼ 1.3%. In all the images North is up and East is on the left.

For spectral analysis, we processed the event files with the *EVIGWEIGHT* task (Arnaud et al. 2001) to correct for vignetting effects. For the background subtraction we used the same background event files used for the images. Spectra were rebinned to achieve a signal-to-noise ratio per bin > 5σ, and the spectral fits were performed simultaneously on the MOS1, MOS2 and pn spectra in the 1 – 9 keV band using XSPEC (Arnaud 1996). The chosen on-axis response files are m1,2_medv9q20t5r6_all_15.rsp for MOS1,2 spectra and epn_ff20_sdY9_medium.rsp for pn spectra. All the reported errors are at 90% confidence, as calculated according to Lampton et al. (1976).

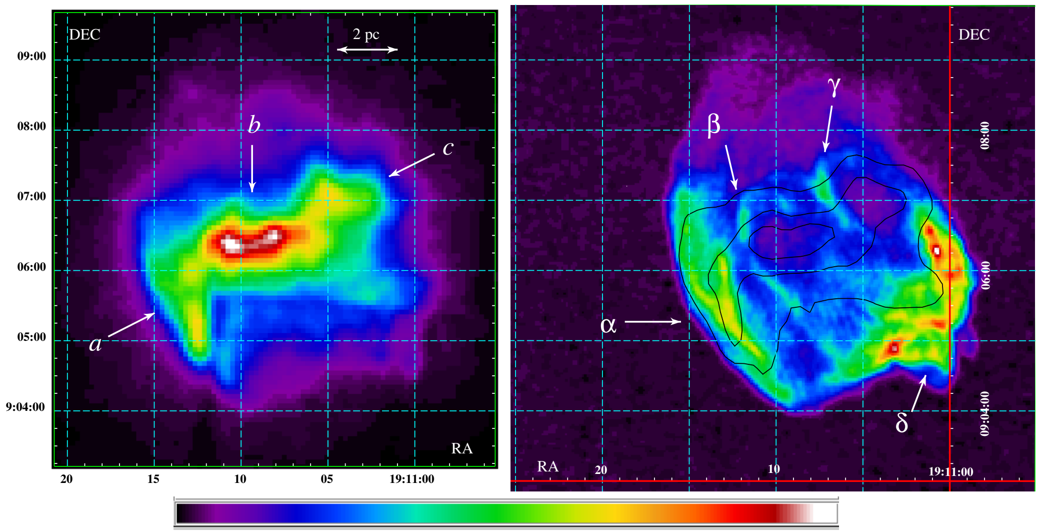

Figure 1. *Left panel:* Vignetting corrected EPIC count rate image of W49B in the 1 – 9 keV band. The image is adaptively smoothed (with signal-to-noise ratio 10) and background-subtracted. The 2 pc scale has been obtained assuming a distance of 8 kpc. The count rate ranges between 0 and 7.2×10^{-3} s^{-1}. *Right panel:* Radio image of W49B at 327 MHz (angular resolution 6″), obtained by Lacey et al. (2001). We have superimposed in black the X-ray contour levels derived from the 1 – 9 keV EPIC image at 25%, 50% and 75% of the maximum. The color bar has a linear scale.

3. X-ray emission

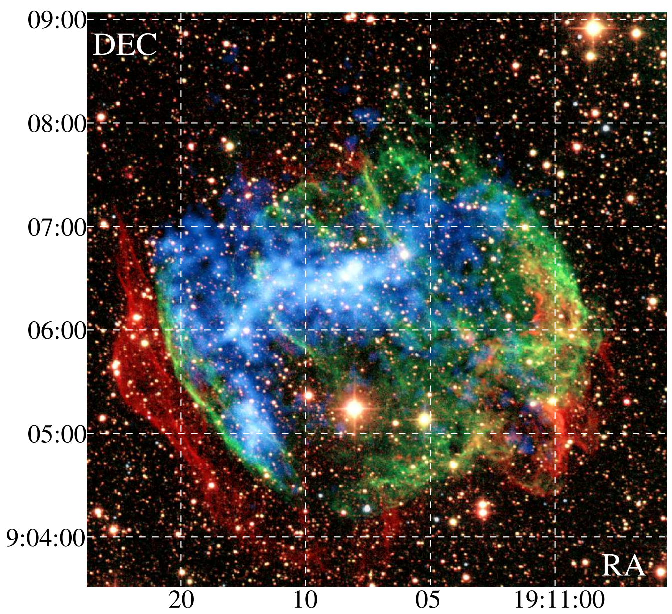

Figure 2. Color composite *Chandra* X-ray image (in blue), infrared 2.12 μm molecular hydrogen (in red), and 1.64 μm [Fe II] (in green) images of W49B (from http://chandra.harvard.edu/press/04_releases/press_060204.html).

The broadband (1 – 9 keV) X-ray morphology of W49B obtained with the EPIC cameras is shown in Fig. 1 (left panel). For comparison, the VLA radio image obtained at 327 MHz by Lacey et al. (2001) is also presented in Fig. 1 (right panel). The X-ray surface brightness of W49B has its maximum at the center of the remnant, and shows an elongated barrel-shaped structure extending for ~ 5 pc along its east-west axis (labelled *b*, see Fig. 1) .

At the eastern end of the remnant there is a bright elongated X-ray structure (labelled *a*, see Fig. 1), running perpendicular to the X-ray barrel and parallel to the radio shell (labelled α, see Fig. 1). The eastern side of W49B is bounded by a large molecular cloud detected in the 2.12 μm molecular hydrogen narrow band image of W49B (Fig. 2). The X-ray barrel *b* lies between two radio structures (β and γ) which are parallel to the radio shell (α) and to the H_2 emission. The positions of these structures (β and γ) are almost coincident with two coaxial ring-like structures observed in the 1.64 μm [Fe II] image of W49B (Fig. 2). The X-ray structures *a* (east) and *c* (west) lie outside these radio structures. No intense X-ray emission has been detected in the south-western region of the shell, where copious radio and [Fe II] emission are observed (δ, see Fig. 1). According to Lacey et al. (2001), there is evidence for stronger interstellar absorption in this direction. It is reasonable to conclude, however, that no hard X-ray emission is present in this region.

3.1. Global spectrum

The impressive global EPIC spectrum of W49B in the 1–9 keV energy band is shown in Fig. 3. The spectrum is dominated by intense emission lines of He-like and H-like ions of Si, S, Ar and Ca and by a huge Fe K emission line blend. A phenomenological modelling of the global spectrum (2 bremsstrahlung for the continuum + narrow gaussians for the lines) allows us to derive the line energies reported in Fig. 3. The emission feature observed at ~ 7.8 keV corresponds to a possible blending of Fe XXV and Ni XXVII K emission lines and is discussed in sect. 3.4. The continuum above 2.3 keV is well described by a thermal bremsstrahlung model with $kT = 1.69$ keV and

$N_H = 5.3 \times 10^{22}$ cm^{-2}; this model has been used to estimate the continuum under the lines given in Table 2. Unlike the *ASCA* spectrum (Hwang et al. 2000), the *XMM-Newton* global spectrum cannot be correctly fitted by a two-component thermal model (reduced $\chi^2 \sim 2.4$). This indicates that the emission originates from physically inhomogeneous regions. Spatially resolved spectral analysis of homogeneous regions is required to correctly reproduce the spectra with 2-component models, as discussed in Sect. 3.3.

In the analysis of the *ASCA* global spectrum of W49B, Hwang et al. (2000) found evidence for the presence of two new emission line features (at $\sim$ 5.7 keV and $\sim$ 6.2 keV) that are not included in the currently available atomic database for X-ray spectral modeling. These were attributed to the He-like Cr transitions (forbidden line at 5.655 keV; resonance line at 5.682 keV) and the He-like Mn transitions (forbidden line at 6.151 keV; resonance line at 6.181 keV). Our *XMM-Newton* data confirm this detection. Modelling the global spectrum of the remnant in the 4.4 – 6.4 keV band with a thermal bremsstrahlung continuum, we found a clear excess in the residuals corresponding to these transitions. These lines can be reproduced by adding two gaussian components to the bremsstrahlung model to determine the line energy and flux. We found, respectively for Cr and Mn, line centroid energy $E_{Cr} = 5.66 \pm 0.01$ keV and flux $F_{Cr} = 2.5 \pm 0.4 \times 10^{-5}$ photons cm^{-2} s^{-1}, $E_{Mn} = 6.19^{+0.01}_{-0.04}$ keV and $F_{Mn} = 1.0 \pm 0.3 \times 10^{-5}$ photons cm^{-2} s^{-1}, in quite good agreement with the values reported by Hwang et al. (2000): $E_{Cr} = 5.69^{+0.02}_{-0.03}$ keV and $F_{Cr} = 3.0^{+0.8}_{-1.1} \times 10^{-5}$ photons cm^{-2} s^{-1}; $E_{Mn} = 6.17 \pm 0.05$ keV and $F_{Mn} = 1.3^{+1.4}_{-0.6} \times 10^{-5}$ photons cm^{-2} s^{-1}. The addition of the Cr gaussian leads to a reduction of χ^2, $\delta\chi^2 = 111$ for 616 d. o. f.; adding the Mn gaussian gives an additional $\delta'\chi^2 = 28$ (to be compared with the values obtained with the *ASCA* spectrum: $\delta\chi^2 = 20$ for 61 d. o. f. and $\delta'\chi^2 = 10$). We found no indication for the presence of the Ti Heα line (at 4.97 keV), obtaining an upper limit for the flux $F_{Ti} < 3.6 \times 10^{-6}$ photons cm^{-2} s^{-1}, that is more stringent that the one reported from ASCA ($F_{Ti} < 2 \times 10^{-5}$ photons cm^{-2} s^{-1}, Hwang et al. 2000). The flux of the Cr and Mn lines contributes $\sim$ 3% of the total flux in the 4.4 – 6.4 band.

3.2. Imaging

The spatially resolved spectral study of the emission in the different lines provides information about the spatial distribution of the synthesized elements and the chemical composition of the X-ray emitting plasma. On the basis of low angular resolution *ASCA* images of W49B, Fujimoto et al. (1995) argued that the sulfur emission, unlike the iron emission, was associated with the outer envelope of the remnant and not related to the bright 4 – 6 keV continuum emission from the center.

To investigate both this claim and the suggested radial stratification of the elements, we produced background- and continuum-subtracted line images of S, Ar, Ca, Fe and Ni lines (see Table 2). Si emission line images, shown in Fig. 6, are discussed in Sect. 3.3.1. The S H-like line image is very similar to the S He-like line image and therefore is not shown in the figure. All the line images present a bright centrally barrel-shaped morphology similar to the 4.4 – 6.2 keV continuum emission, as shown in Fig. 4. Overall, there are no significant differences between the morphologies in the Si, S, Ar, Ca and Fe lines (although some detailed structures may differ as we will discuss later). This result is not in agreement with the line imaging results obtained for the lower-Z elements with *ASCA* data (see Fig. 4 in Fujimoto et al. 1995).

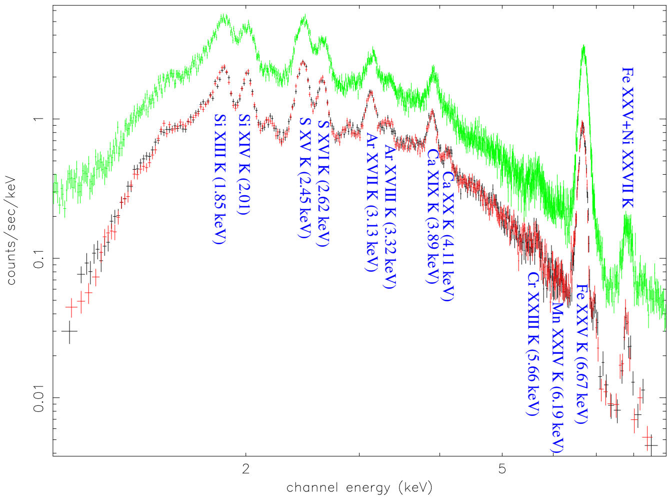

Figure 3. pn (upper) and MOS (lower) global spectra of W49B in the 1 – 9 keV energy band, extracted from a circular region covering the entire remnant (of radius 3.3′ corresponding to $\sim$ 7.7 pc). Line energies have been determined using narrow gaussian components on top of a thermal bremsstrahlung continuum. Note that to reproduce the continuum at energies below the Si K lines, an additional bremsstrahlung component is required.

A detailed analysis of the Fe K line image in Fig. 4 (lower left panel) shows that the iron emission differs from that lower-Z elements in the western part of the remnant. In particular, regions 6 and 7 do not have significant Fe line emission, while they do have significant emission from Si, S, Ar and Ca. The lower statistic Fe XXV+Ni XXVII image of Fig. 4 (lower right panel) presents a morphology that is fully consistent with that of the Fe K image.

To disentangle higher element abundances in the bright line image structures from higher emission measure (which might be caused by either higher density or higher emission volume), we produced equivalent width maps as shown in Fig. 5. These depend linearly on the abundances, but are also affected by the temperature, column density and ionization age. These images have been constructed by dividing the background- and continuum-subtracted line images by the corresponding underlying continuum. Before the division, the estimated continuum map was adaptively smoothed using the same template used for the background- and continuum-subtracted line images. As explained in Sect. 2, the underlying continuum is estimated from continuum regions adjacent to the line emission, and assumes that the continuum has a uniform spectral slope over the entire SNR. As shown in Fig. 5, the S map is clearly different from the other maps, but the equivalent width images of Ar, Ca, Fe and Fe+Ni all show similar features. In particular, all

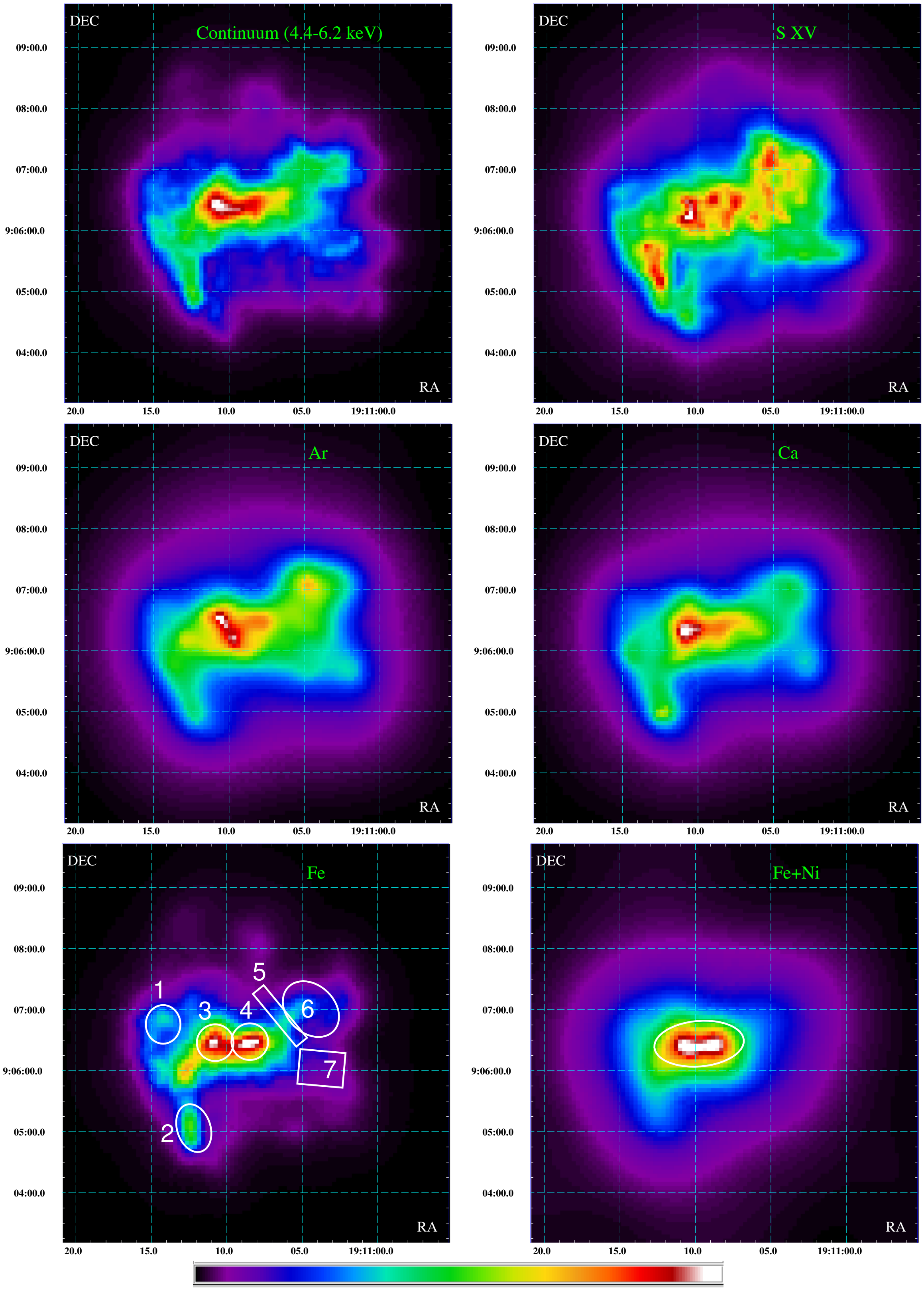

Figure 4. Vignetting corrected and continuum-subtracted EPIC count rate images of the continuum (4.4 – 6.2 keV, *upper left*); S XV K (2.35 – 2.53 keV, *upper right*); Ar XVII K (3.05 – 3.2 keV, *central left*); Ca XIX K (3.8 – 4.0 keV, *central right*); Fe XXV K (6.45 – 6.9 keV, *lower left*) and Fe XXV+Ni XXVII K (7.65 – 8.0 keV, *lower right*). All images are adaptively smoothed with signal-to-noise ratio 10. The 7 regions selected for spatially resolved spectral analysis are shown in the Fe XXV K line image, while the ellipse in the Fe XXV+Ni XXVII K line image indicates the region used for the detection of the Ni line (Sect. 3.4). The count rates range between 0 and: 8.6×10^{-4} s^{-1} (continuum); 3.4×10^{-4} s^{-1} (S); 1.7×10^{-4} s^{-1} (Ar); 1.9×10^{-4} s^{-1} (Ca); 7.0×10^{-4} s^{-1} (Fe); 2.1×10^{-5} s^{-1} (Fe+Ni). The color bar has a linear scale.

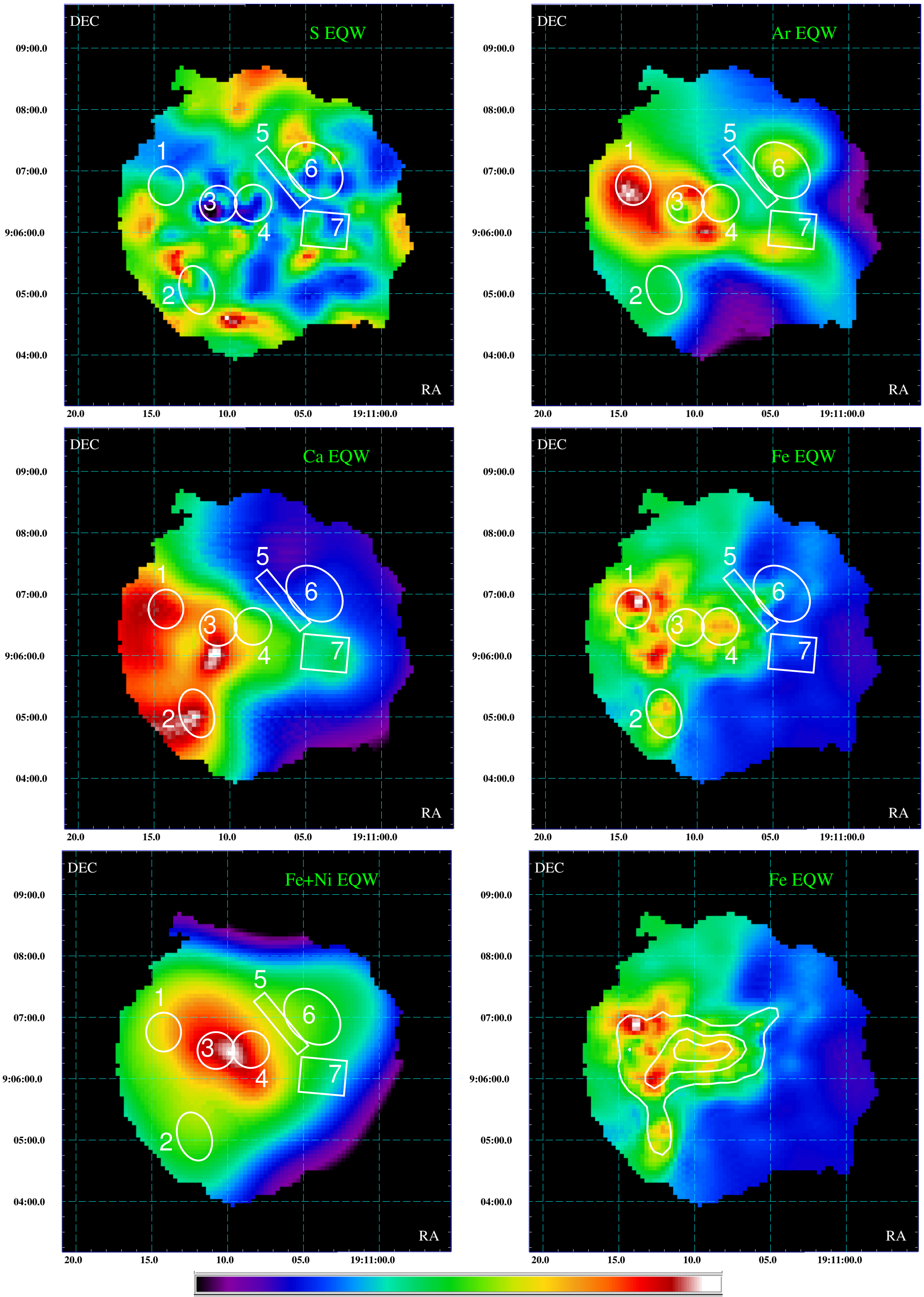

Figure 5. Equivalent width maps of the S He-like and H-like line emission in the 2.35 – 2.7 keV band (*upper left*); of the Ar XVII K blend (3.05 – 3.2 keV, *upper right*); of Ca XIX K (2.35 – 2.7 keV, *central left*); of Fe XXV K (6.45 – 6.9 keV, *central right*) and of the Fe XXV+Ni XXVII K emission lines in the 7.65 – 8.0 keV band (*lower left*). In the *lower right* panel we have overlaid on the Fe XXV K equivalent width map the 75%, 50% and 25% contour levels of the corresponding line image (Fig. 4, lower left panel). The ranges of the equivalent width maps are: 0.245 – 0.6 keV (S); 0.07 – 0.13 keV (Ar); 0.085 – 0.18 keV (Ca); 0 – 12.1 keV (Fe); 0.315 – 1.4 keV (Fe+Ni).

Table 2. Parameters used for the production of the line images of Fig. 4 and the equivalent width maps of Fig. 5.

Emission line	Line energy band (keV)	Continuum energy band (keV)
S XV Kα	2.35 – 2.53	2.75 – 3.0
S XVI Kα	2.58 – 2.7	2.75 – 3.0
Ar XVII Kα	3.05 – 3.2	2.75 – 3.0
Ca XIX Kα	3.8 – 4.0	3.45 – 3.7
Fe XXV Kα	6.45 – 6.9	4.4 – 6.2
Fe XXV+Ni XXVII K	7.65 – 8.0	7.05 – 7.5

these maps show higher equivalent widths in the central and eastern parts of the remnant than in the western part, with maxima corresponding approximately to regions 1 and 3. This is particularly true for iron. In the Ar map there is an indication of non-negligible equivalent widths in the western regions 6 and 7.

As the S H-like and He-like line images are very similar, we used the combined 2.35 – 2.7 keV band to improve the statistics of the sulfur equivalent width map as shown in Fig. 5 (upper left panel). The map appears patchy and shows no clear structures. Given the relatively low line energies, the map may be affected by local variations of N_H, as we shall see in Sect. 3.3.1.

In conclusion, the line emission maps of all the observed elements show a centrally elongated bright structure in good agreement with the morphology of the continuum. The equivalent width images indicate that Ar, Ca and Fe may be more abundant in the central and eastern parts of the remnant than in the west. The high values of the equivalent width are therefore not restricted to the barrel-like structure, but extend to the eastern side of the remnant, as illustrated in Fig. 5 (lower right panel), where we show the contours of the iron line image superimposed on the iron equivalent width map. A clear drop-off of the equivalent width is observed towards the western side. This effect is particularly strong for iron, and less pronounced for the lower-Z elements which show significant equivalent widths in the west. While we thus find an East/West abundance anisotropy, we find no clear evidence for radial stratification of the elements.

3.3. Spatially resolved spectral analysis

To quantify the equivalent width map results for the element distributions, we performed a spatially resolved spectral analysis that allowed us to study in detail the physical and chemical characteristics of the plasma in different parts of the remnant. In particular, we analyzed the spectra extracted from seven fairly homogeneous regions shown in Fig. 4 (lower left panel) and in Fig. 5. While this set of regions does not cover the entire remnant, it does allow us to study the spatial variations of the spectral properties in the X-ray emitting plasma. In order to analyze spectra extracted from physically uniform regions, we produced a MOS mean photon energy map (i.e., an image where each pixel holds the mean energy of the detected MOS photons) in the continuum band 4.4 – 6.2 keV. The shape and size of the seven regions were chosen in order to have very small fluctuations of the mean photon energy ($\sim 1\%$) and a sufficient number of photons.

Regions 1 and 2 are located on the X-ray eastern elongated structure along the radio shell (labelled a/α in Fig. 1), respectively at its northern and southern ends. They both exhibit high values in the equivalent width maps.

Regions 3 and 4 cover the brightest part of the centrally barrel-shaped X-ray structure: region 3 corresponds to the maximum of the continuum emission in the 4.4 – 6.2 keV band (Fig. 4, upper left panel), region 4 corresponds to the highest Fe K line emission region (Fig. 4, lower left panel).

Region 5 follows the western radio structure γ (Fig. 1). Region 6 covers the western X-ray structure c and, finally, region 7 lies on the faint south-western structure that is seen in the continuum and K line emission of S, Ar, Ca, but not of iron.

3.3.1. Spectral modelling and results

We first modelled the extracted spectra using XSPEC with a single MEKAL model of an optically-thin thermal plasma in collisional ionization equilibrium (Mewe et al. 1985, Mewe et al. 1986, Liedahl et al. 1995). Good fits to the spectra require non-solar abundances for Si, S, Ar, Ca and Fe. All other element abundances were fixed at their solar values. To account for the contribution from the Cr line (Sect. 3.1), we added a narrow gaussian component with fixed energy; it was not necessary to account for the Mn line. We also added a systematic 5% error term to reflect the estimated 5-10% uncertainties in the calibration of the instrumental effective area. The reduced χ^2 values obtained using the two MOS and the pn cameras range from 1.3 (with 354 d.o.f.) for region 5, to 1.7 (445 d.o.f.) for region 2. Above 2 keV, the models describe the continuum and emission line spectra quite well, but these single-temperature models severely underpredict the Si XIII Kα line, as illustrated in Fig. 7 (left panel). The best-fit parameters for these fits are thus not reported here. The same problem was encountered by Hwang et al. (2000) in the modelling of the *ASCA* global spectrum. We found that the quality of the fits does not significantly improve if a single non-equilibrium ionization (NEI) model is used instead.

We obtained a good description of the spectra by adding a second collisional ionization equilibrium thermal MEKAL component. We require the two components to have the same abundances and to be absorbed by the same interstellar column density. The spectra are also well-described if the soft component has solar abundances and is in nonequilibrium ioniza-

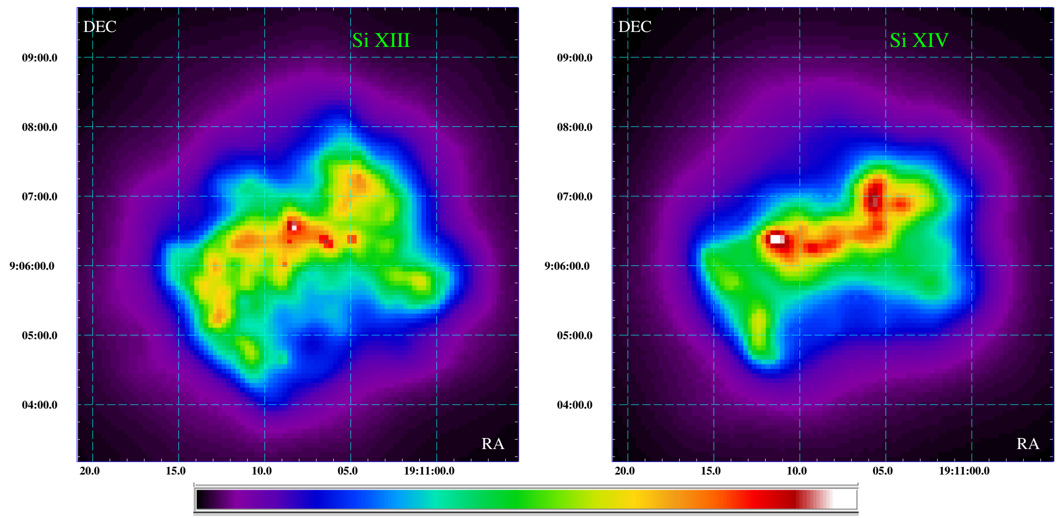

Figure 6. Vignetting corrected and continuum-subtracted EPIC count rate image of the Si XIII Kα ($1.77-1.9$ keV, *left panel*) and Si XIV Kα ($1.96-2.06$ keV, *right panel*). The images are adaptively smoothed with signal-to-noise ratio 10. The count rates range between 0 and 2.3×10^{-4} s^{-1} for Si XIII and 1.7×10^{-4} s^{-1} for Si XIV. The color bar has a linear scale.

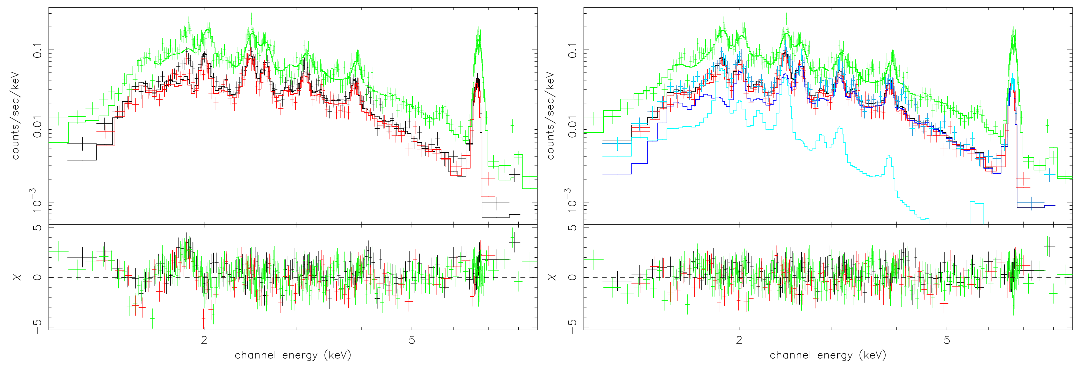

Figure 7. pn (upper) and MOS (lower) spectra of region 2 with the corresponding best-fit model and residuals obtained with one thermal component (left panel) and with two thermal components (right panel). The contribution of the two components for the MOS camera is indicated in the right panel in cyan for the cooler component and blue for the hotter component.

tion (PSHOCK model). In this case the temperatures of the two components (NEI+CIE) are comparable to those obtained for the two CIE components, but the fits give somewhat higher chi-squared values. For example, in region 2: $\chi^2_{NEI+CIE}=529.7$ (with 442 d. o. f.) and $\chi^2_{2CIE}=506.7$ (443); in region 4: $\chi^2_{NEI+CIE}=821.2$ (673) and $\chi^2_{2CIE}=793.5$ (674); in region 6: $\chi^2_{NEI+CIE}=1064.1$ (843) and $\chi^2_{2CIE}=1059.3$ (844). We therefore adopt the two CIE component model hereafter, while cautioning the reader that the high interstellar absorption complicates the description of the soft component and hence the discrimination between these two models.

Fig. 7 shows a representative spectrum, extracted from region 2, with best-fit model and residuals for two thermal components (right panel), and for comparison, a single thermal component (left panel). The best-fit parameters for all seven spectral regions are given in Table 3.

The values of $N_{\rm H}$ in the different spectral regions range approximately from 4.2×10^{22} cm^{-2} to 4.9×10^{22} cm^{-2} (compared with the global $N_{\rm H}=5.0^{+0.3}_{-0.2}\times10^{22}$ cm^{-2} estimated by Hwang et al. 2000). To produce the line and the equivalent width images (see Sect. 3.2), we estimate the continuum contribution under the lines by assuming a uniform absorbed slope of the continuum based on the global spectrum of W49B. For low energy lines, spatial variation of the column density over the remnant can thus introduce errors in the line and equivalent width images. In particular, where $N_{\rm H}$ is higher than its global averaged value, we may overestimate the continuum under the line and hence underestimate the equivalent width. We observe this kind of effect in the S equivalent width image (Fig. 5, upper left panel), where there is a minimum in region 3 with a mean value of 0.32 keV, corresponding to the highest value of the column ($N_{\rm H}=4.8^{+0.1}_{-0.2}$), and a higher mean equivalent width of 0.4 keV in region 2 which has a lower column ($N_{\rm H}=4.22^{+0.08}_{-0.05}$).

Variations in column density may also affect the Si images, but in this case there is no a clear relation between such variations and inhomogeneities in the equivalent width map. This probably indicates that other effects are also present. As explained above, a single temperature model provides a good overall description of the spectra in the $1-9$ keV band, but fails to reproduce the observed Si line flux in the narrow energy range $1.7-1.9$ keV. It is therefore possible that the Si He-like emission originates predominantly in a plasma with different physical conditions than that responsible for the other emission lines. As shown in Fig. 6, the He-like line morphology resembles that of the Si H-like emission as well as the S, Ar and Ca line emission. The Si equivalent width maps (not presented here) have irregular patchy features at odds both with those seen for the other elements, and with the spatially resolved spectral analysis. This is probably because the continuum of the hard component is not negligible at low energies, even though the Si He-like line emission itself is associated with the soft thermal component (see the right panel of Fig. 7).

We observe larger variations for the temperature of the hotter component kT_2 (1.75 – 3.3 keV) than for the cooler component kT_1 (0.7 – 1.05 keV), but do not measure any radial temperature structure (see Table 3). The temperature of the hotter component is at a maximum in Region 1 at kT_2, and decreases significantly moving southward along the X-ray elongated a structure to region 2. This temperature also decreases towards the western side of the remnant (from region 3 to region 6). We observe that the difference between the continuum surface brightness of regions 3 (i. e. the brightest region in the continuum band 4.4 – 6.2 keV) and region 4 is caused by the higher temperature in region 3, and not by differences in the emission measure.

In Table 3, the parameter EM indicates the values of the emission measure per unit area, which is the product of the square of the particle density times the extension of the plasma along the line of sight. These values are in the range $0.3 - 1.7 \times 10^{20}$ cm^{-5} for the cooler component, and $0.4 - 3.5 \times 10^{20}$ cm^{-5} for the hotter component. In region 6 we have the highest values for both EM_1 and EM_2. Associated with the decreasing trend of T_2, we note that in region 6 the corresponding emission measure EM_2 is slightly higher than in regions 3 and 4.

We used the best-fit values of temperature and emission measure to derive the plasma density (indicated with n in Table 3) and the filling factor (f) of each component, obtained as in Bocchino et al. (1999). These quantities were derived assuming pressure equilibrium between the two components and assuming that in each spectral region the extension of the X-ray emitting plasma is equal to the length of the chord intercepted by the radio shell (approximated as a sphere with angular radius $\phi = 2.15'$) along the line of sight. The filling factor of the cool component is $\lesssim 0.1$, and the densities of the two components are almost uniform across the remnant.

We found significant element overabundances in all the spectral regions: all the elements have fitted abundances > 1.5 (at 90% confidence level) with respect to their solar value. This attests to the origin of the emission in the ejecta. Moreover, higher abundance values are found for the central and eastern regions compared to the western regions, in good agreement with the results of our image analysis. All abundances are lower in regions 5, 6, and 7, with the largest decrease observed for the Fe abundance, as expected. For example, the ratio $(Ar/Ar_\odot)/(Fe/Fe_\odot)$ is 0.7 ± 0.1 in region 4 and 1.8 ± 0.3 in region 6, and the ratio $(Ca/Ca_\odot)/(Fe/Fe_\odot)$ is 1.2 ± 0.2 in region 4 and $1.8^{+0.3}_{-0.2}$ in region 6. This is in agreement with the considerations discussed at the end of Sect. 3.2, where regions 6 and 7 show low equivalent widths for iron, but nonnegligible line emission and line equivalent widths for the lower-Z elements. All the abundances reported in Table 3 are given as the ratio of the number density of the respective element to the number density of hydrogen expressed in units of the solar value of this ratio. In a pure-ejecta plasma (where hydrogen emission is negligible) this ratio would be ill-defined, and the spectral shape would depend only on the relative abundances of the heavy elements. We verified that this is not the case for our fits. In fact if we scale all the abundances by the same factor f we obtain significantly higher χ^2 values for $f \gtrsim 1.5$. Therefore the abundances in Table 3 are well defined and above solar.

In each spectral region we also obtained another χ^2 minimum with $kT_1 \sim 0.2$ keV. This value is in agreement with the results obtained with the *ASCA* data by Hwang et al. (2000) and Kawasaki et al. (2005). In this case, however, we found very high values for the emission measure per unit area of the cool component ($EM_1 \gtrsim 10^{22}$ cm^{-5}), which would imply unrealistically high values for the filling factor ($f_1 \sim 0.5$) and the density ($n_1 \sim 50$ cm^{-3}). In what follows, we will therefore discuss only the results presented in Table 3.

3.4. Evidence for Ni overabundance

Thanks to the high *XMM-Newton* effective area at high energies it was possible to detect a strong emission feature at ∼ 7.8 keV, with possible contributions from both Fe XXV and Ni XXVII. The Ni XXVII emission line has been previously detected in only in one SNR, Cas A (Bleeker et al. 2001, Willingale et al. 2002). This emission blend can be used to set constraints on the Ni abundance in W49B. Since the photon statistics for the seven individual spectra do not allow us to resolve the features in the 7.65 – 8.0 keV band in detail, we extracted the spectrum from the larger elliptical region shown in Fig. 4 (lower right panel). This region covers the area of highest surface brightness in the 7.65 – 8.0 keV band. We fitted the spectrum in the 1 – 9 keV band with the 2-component thermal model used for the spatially resolved spectral analysis. Table 4 gives the best-fit parameters derived both by fixing the Ni abundance to the solar value (second column) and by fitting the Ni abundance as a free parameter (third column). We can better reproduce the Fe XXV and Ni XXVII K line blends by fitting for the Ni abundance. The F-test gives the probability that the improvement of the fit is insignificant as $< 10^{-10}$. We conclude that there is convincing evidence for Ni overabundance ($Ni/Ni_\odot = 10^{+2}_{-1}$) in the centrally barrel-shaped structure of W49B.

3.5. Overionization

Through their analysis of the *ASCA* global spectrum, Kawasaki et al. (2005) claimed the presence of "overionized" plasma in W49B. In particular, they measured the intensity ratio of the H-like to the He-like Kα lines of Ar and Ca to obtain the ionization temperature T_z, and found that T_z is higher than the electron temperature T_e estimated from the continuum of the X-ray spectrum. We performed the same analysis by modelling the *XMM-Newton* global spectrum in the 2.75 – 6.0 keV band. We model the continuum and estimate T_e with a zero metal-

Table 3. Best-fit parameters for the spectra extracted in the seven regions shown in Fig. 4 (lower left panel), described with two thermal components in collisional ionization equilibrium. All errors are at the 90% confidence level.

Parameter	Region 1	Region2	Region 3	Region 4	Region 5	Region 6	Region 7
$N_{\rm H}$ (10^{22} cm^{-2})	4.5 ± 0.1	$4.22^{+0.08}_{-0.05}$	$4.8^{+0.1}_{-0.2}$	4.5 ± 0.1	$4.3^{+0.2}_{-0.1}$	4.61 ± 0.05	$4.36^{+0.08}_{-0.09}$
kT_1 (keV)	$0.90^{+0.08}_{-0.06}$	$0.75^{+0.03}_{-0.05}$	$0.92^{+0.06}_{-0.08}$	0.8 ± 0.1	$0.96^{+0.09}_{-0.09}$	$0.78^{+0.06}_{-0.04}$	$0.82^{+0.09}_{-0.06}$
EM_1^* (10^{20} cm^{-5})	$0.5^{+0.2}_{-0.1}$	$1.16^{+0.1}_{-0.09}$	1.2 ± 0.2	$1.3^{+0.3}_{-0.3}$	$0.8^{+0.3}_{-0.2}$	$1.1^{+0.4}_{-0.2}$	$0.92^{+0.1}_{-0.05}$
kT_2 (keV)	$3.0^{+0.4}_{-0.2}$	$2.19^{+0.1}_{-0.06}$	2.6 ± 0.2	$2.35^{+0.12}_{-0.09}$	$2.2^{+0.2}_{-0.2}$	$1.77^{+0.03}_{-0.09}$	2.00 ± 0.04
EM_2^*(10^{20} cm^{-5})	0.5 ± 0.1	1.1 ± 0.1	$1.8^{+0.1}_{-0.1}$	$1.95^{+0.1}_{-0.08}$	1.4 ± 0.3	$2.2^{+0.3}_{-0.1}$	1.3 ± 0.1
$Si/Si_\odot$	2.2 ± 0.4	$3.4^{+0.2}_{-0.4}$	3.7 ± 0.4	2.9 ± 0.3	$2.4^{+0.3}_{-0.5}$	2.3 ± 0.1	$2.1^{+0.3}_{-0.2}$
$S/S_\odot$	4.1 ± 0.5	4.1 ± 0.3	$4.6^{+0.3}_{-0.6}$	$3.6^{+0.3}_{-0.4}$	$2.7^{+0.3}_{-0.5}$	$2.4^{+0.2}_{-0.1}$	2.8 ± 0.3
$Ar/Ar_\odot$	$5.6^{+1.1}_{-0.9}$	3.8 ± 0.6	$4.9^{+0.8}_{-0.6}$	$4.1^{+0.3}_{-0.7}$	2.6 ± 0.6	2.8 ± 0.3	$3.4^{+0.3}_{-0.5}$
$Ca/Ca_\odot$	8 ± 1	$6.6^{+0.9}_{-0.8}$	7 ± 1	$6.9^{+0.7}_{-0.9}$	$4.7^{+0.8}_{-0.9}$	$4.4^{+0.4}_{-0.5}$	$5.2^{+0.5}_{-0.7}$
$Fe/Fe_\odot$	$5.2^{+0.6}_{-0.4}$	5.1 ± 0.3	$5.1^{+0.4}_{-0.6}$	$5.6^{+0.4}_{-0.3}$	$2.6^{+0.2}_{-0.3}$	$2.5^{+0.1}_{-0.2}$	$1.6^{+0.2}_{-0.1}$
χ^2/d. o. f.	298.8/244	506.7/443	800.0/646	793.5/674	403.2/352	1059.3/844	566.3/434
f_1	$0.08^{+0.03}_{-0.04}$	$0.11^{+0.04}_{-0.03}$	0.08 ± 0.04	0.08 ± 0.03	$0.10^{+0.06}_{-0.05}$	$0.09^{+0.06}_{-0.04}$	$0.11^{+0.04}_{-0.03}$
n_1 (cm^{-3})	6^{+3}_{-2}	7^{+2}_{-1}	7^{+4}_{-2}	8 ± 2	5^{+3}_{-2}	7^{+4}_{-2}	$5.5^{+3}_{-0.9}$
n_2 (cm^{-3})	$1.8^{+0.3}_{-0.2}$	$2.5^{+0.2}_{-0.1}$	2.6 ± 0.2	$2.6^{+0.3}_{-0.1}$	2.3 ± 0.2	$3.0^{+0.8}_{-0.2}$	2.3 ± 0.2

* Emission measure per unit area.

Table 4. Best-fit parameters for the spectrum extracted from the elliptical region shown in Fig. 4 (lower right panel) and reproduced by two thermal components in collisional ionization equilibrium. All errors are at the 90% confidence level.

Parameter	$Ni/Ni_\odot = 1$	Ni thawed
$N_{\rm H}$ (10^{22} cm^{-2})	$4.60^{+0.06}_{-0.03}$	$4.68^{+0.06}_{-0.02}$
kT_1 (keV)	$0.87^{+0.04}_{-0.02}$	$0.86^{+0.02}_{-0.05}$
EM_1^* (10^{20} cm^{-5})	$1.13^{+0.04}_{-0.02}$	$1.1^{+0.1}_{-0.2}$
kT_2 (keV)	$2.35^{+0.02}_{-0.03}$	$2.2^{+0.2}_{-0.1}$
EM_2^* (10^{20} cm^{-5})	$1.79^{+0.06}_{-0.04}$	$1.82^{+0.06}_{-0.05}$
$Si/Si_\odot$	$3.3^{+0.1}_{-0.3}$	3.3 ± 0.2
$S/S_\odot$	3.7 ± 0.1	$3.7^{+0.1}_{-0.2}$
$Ar/Ar_\odot$	$4.2^{+0.4}_{-0.2}$	$4.2^{+0.3}_{-0.4}$
$Ca/Ca_\odot$	6.3 ± 0.5	6.4 ± 0.5
$Fe/Fe_\odot$	$5.5^{+0.1}_{-0.2}$	$6.0^{+0.1}_{-0.2}$
$Ni/Ni_\odot$	1	10^{+4}_{-1}
χ^2/d. o. f.	1847.8/1327	1584.3/1326

* Emission measure per unit area.

licity VMEKAL component and include four narrow gaussian components to model the Ar and Ca lines and a fifth gaussian component for the Cr line. We considered absorption column densities of $N_H = 4.6 \times 10^{22}$ cm^{-2} and $N_H = 5.23 \times 10^{22}$ cm^{-2} (the value adopted by Kawasaki et al. (2005)). For those column densities, we obtained electron temperatures of $kT_e = 1.80 \pm 0.03$ keV and $1.66^{+0.02}_{-0.01}$ keV, respectively. We find no evidence of overionization for Ar, given the respective ionization temperatures of $kT_z = 1.68 \pm 0.07$ and $kT_z = 1.64^{+0.08}_{-0.05}$. For Ca, the ionization temperature does seem higher than the continuum temperature: $kT_z = 2.0^{+0.1}_{-0.05}$, with $N_H = 4.6 \times 10^{22}$ cm^{-2}, and $kT_z = 2.04^{+0.1}_{-0.08}$, with $N_H = 5.23 \times 10^{22}$ cm^{-2}. However, we caution the reader that these estimates may not be reliable because the global spectrum originates from physically non-uniform regions of W49B that have different temperatures and abundances. A case in point in that the estimates of the electron temperatures obtained from the global spectrum are significantly lower those obtained from our spatially resolved spectral analysis of homogeneous regions (see Sect. 3.3 and kT_2 values in Table 3). We therefore repeated our analysis for the more uniform central region indicated by a white ellipse in the lower left panel of Fig. 5. This is where the overionization effects are expected to be strongest in the scenario proposed by Kawasaki et al. (2005). Our analysis shows that these effects are not present. Using the same model described above in the 2.75-6.0 keV band, we found for $N_H = 4.6 \times 10^{22}$ cm^{-2} and $N_H = 5.23 \times 10^{22}$ cm^{-2}: respective electron temperatures of $kT_e = 2.4 \pm 0.1$ keV and $kT_e = 2.25^{+0.08}_{-0.1}$, Ar ionization temperatures of $kT_z = 1.9^{+0.1}_{-0.2}$ and $kT_z = 1.8 \pm 0.1$, and Ca ionization temperatures of $kT_z = 2.3^{+0.1}_{-0.3}$ and $kT_z = 2.2 \pm 0.2$. Given that kT_z is always slightly lower than, or consistent with kT_e, we conclude that there is no indication of overionization in the central region of W49B.

4. Discussion

On the basis of low angular resolution *ASCA* line images, Fujimoto et al. (1995) argued for stratification of the SN ejecta in W49B, with iron confined to the inner region and lower-Z elements (Si and S) forming an outer envelope. This hypothesis was supported by the analysis of the global spectrum, with the intensity ratios of Lyα and Heα giving different ionization ages for Si, S, Ar and Ca. Hwang et al. (2000) pointed out that while this conclusion is compatible with the *ASCA* spectrum, no difference in the ionization ages is required if the data are modelled with a two-component thermal plasma. The analysis of *XMM-Newton* data allowed us to discriminate between these two scenarios. Our spatially resolved spectral analysis has shown that a correct fit of the spectra requires two thermal components and that these two components are compatible with collisional ionization equilibrium, both at the center and in the outer parts of the remnant. Moreover, as explained in Sect. 3.2, our line images and equivalent width maps exclude a radial stratification of the elements in the ejecta, with Fe K emission confined to the inner part of the X-ray emitting region and lower-Z emission lines originating in an outer shell. In fact, both the central barrel-shaped structure and the eastern elongated structure of the SNR have high abundances of Ar, Ca and Fe, while the western part has lower abundances.

The physical conditions of the plasma are not uniform in W49B. The highest temperatures are found in the northern end of the elongated eastern structure (labelled *a*) and in the central barrel-shaped structure (labelled *b*). The lowest temperatures are found in the western part of W49B and in the south-eastern zone. Assuming pressure equilibrium between the two components, no significant variations in the plasma density across the remnant are observed. The observed X-ray emission originates in the SN ejecta, and Si, S, Ar, Ca, Fe and Ni are all highly overabundant with respect to their solar values. They have almost the same values in structures *a* and *b*, and are lower (but still overabundant) in structure *c*. No clear evidence for X-ray emission from the shocked ambient medium is present. In fact, the results of the spatially resolved spectral analysis suggest that the both the X-ray emitting components are associated with overabundant plasma. This is in agreement with the similarity of the morphology between the Si He-like emission blend (associated with the cooler component) and the other emission blends (associated with the hotter component). As explained in Sect. 3.3, however, the high absorption column inhibits the possibility of a detailed study of the soft component in that it is not easy to determine its morphology. Furthermore, the contribution of the hot component is significant even below 1.7 keV, so that it is not possible to produce a clean image of the soft component. We therefore cannot rule out the possibility that the soft component may be associated with the shocked circumstellar or interstellar medium.

It is interesting to consider to what extent the complex morphology of W49B, and the inhomogeneities in temperature and abundance, are caused by the dynamics of the SN explosion or by the remnant's interaction with its environment. Recent 2.12 micron infrared imaging observations have revealed a shocked molecular H_2 cloud that confines the remnant (Fig. 2). The circular distribution of the molecular cloud around the SNR has likely been shaped by strong stellar winds from the progenitor star pushing out the ambient interstellar material to its current location and forming a cavity. Infrared [Fe II] observations at 1.64 μm reveal a barrel-shaped structure with four coaxial rings of warm gas, which has been interpreted as residuals of a strong stellar wind (Keohane et al. 2004).

The morphology of the eastern region of W49B has clearly been shaped by the ambient molecular cloud. Despite their similar abundance values, the eastern *a* and central *b* regions have very different morphologies. The fact that region *a* is almost perpendicular to region *b* is probably due to its confinement by the large H_2 cloud to the east. The [Fe II] observations show that the cavity is an inhomogeneous environment for the supernova remnant expansion.

In contrast, there are no observed interstellar structures that might have shaped the elongated structure of the central X-ray barrel *b*. This centrally barrel-shaped structure thus may have been produced directly by the supernova explosion or by pre-existing structures in the ambient stellar wind material.

The central barrel morphology seen in the *Chandra* Fe K image has been attributed to a bipolar jet, and taken as evidence that W49B is a $\gamma-$ray burst (GRB) remnant[1]. The presence of such an elongated morphology, however, does not necessarily reflect a jet-like explosion. A similar elongated central bright structure has been observed with *Chandra* in the G292.08+1.8 remnant, but Park et al. (2004) showed that its emission is associated with normal chemical composition plasma that originates in shocked dense circumstellar material rather than shocked ejecta. Unlike for G292.08+1.8 SNR, our analysis suggests that the X-ray emission in the central X-ray barrel of W49B is dominated by ejecta, although we cannot rule out the possibility that the soft component comes from solar abundance material. The scenario proposed for G292.08+1.8 can nevertheless be invoked for W49B. It is possible that the barrel-like X-ray emission reflects the morphology of the ambient medium across the remnant. While no dense structures are visible toward the North and South of W49B (as shown in the infrared image of Fig. 2), we may assume the ambient medium to be enhanced in the central zone, forming a torus-like structure all across W49B. According to this scenario, the cold component may be associated with the thin belt of material heated by the transmitted shock travelling into the ISM structure. This would explain the low values of the filling factor of the soft component. The hot component is associated with the ejecta interacting with the reflected shock. In this case, only the material expelled in the plane of the torus is interacting with the the reverse shock and heated by it. Notice, however, that according to our estimates of the plasma density for the spectral regions, the total mass of the ejecta in the hot component in these regions is ~ 8 $M_\odot$. This indicates that if we assume that we are observing only a small fraction of the ejecta we probably overestimate the total expelled mass.

Another possibility is that the barrel is associated with a bipolar ejecta jet interacting with the cavity wall visible at the eastern end of the remnant. In this case we have to assume that the density contrast has driven a very strong reverse shock which has now reached the center of W49B. Moreover, we have found that structures *a* and *b* have similar abundance values and therefore, that *a* could be considered as the head of the eastern jet. The scenario that emerges is that this jet has been distorted to deviate mostly southwards by its impact with the H_2 wall. In this framework, we would have a highly anisotropic bipolar jet, where the eastern arm is significantly more extended, hot and Fe-rich than the western one.

Jet-like explosions have been investigated as possible mechanisms for $\gamma-$ray bursts (GRB) because a spherically symmetric GRB would require an extremely large energy (several times the solar rest mass). A link between very energetic SNe and GRBs has been found by Galama et al. (1998), who showed that the bright type Ic SN 1998bw (with an estimated energy $E \sim 3 \times 10^{52}$ erg, Iwamoto et al. 1998) is the probable optical counterpart of the $\gamma-$ray burst GRB 980425. Observations of SN 1998bw have shown strong indications of asphericity in the explosion (Mazzali et al. 2001). Indications of aspherical explosions have also been found in many other

[1] http://chandra.harvard.edu/press/04_releases/press_060204.html

hypernovae, i. e. supernova explosions with $E \gtrsim 10^{52}$ erg (for a review on hypernovae see Nomoto et al. 2003).

The relationship between asymmetric hypernovae and GRB is in agreement with the collapsar model (MacFadyen & Woosley 1999), in which the collapse of a massive rotating core can generate a black hole and supersonic jets which propagate through the star. The nebular spectrum of SN 1998bw is well reproduced by such a model. Khokhlov et al. (1999) have shown that this mechanism produces a highly aspherical explosion with bipolar fast jets. A bipolar explosion does not necessarily imply a GRB, however, because a high explosion energy ($\gtrsim 10^{52}$ erg) is also required.

To investigate the possibility that W49B is a GRB remnant, we compared the abundance values found in the *a* barrel (see Table 4) with those obtained from models of explosive nucleosynthesis in bipolar explosions by Maeda & Nomoto (2003). In particular, we compared the expected and observed ratios $(X/X_\odot)/(Fe/Fe_\odot)$ for $X = Si, S, Ar, Ca, Cr, Mn$ and Ni (for Cr and Mn we assumed the same ratios as observed for Ar, in agreement with the estimates given in Hwang et al. 2000). None of the models can reproduce the entire observed abundance pattern. The hypernova models with zero age main sequence progenitor mass $M_{ZAMS} = 40\mathrm{M}_\odot$ and explosion energy $E > 10^{52}$ erg are strongly in disagreement with the observed values (with very large discrepancies for the Si, S and Ar abundances). We obtained better results with the less energetic models 25A ($E = 6.7 \times 10^{51}$ and $M_{ZAMS} = 25\mathrm{M}_\odot$) and 25B ($E = 0.6 \times 10^{51}$ and $M_{ZAMS} = 25\mathrm{M}_\odot$). We also found relatively good agreement with the spherical explosion model 25Sa ($E = 1 \times 10^{51}$ and $M_{ZAMS} = 25\mathrm{M}_\odot$). The predicted values of these three models and our observational findings are summarized in Fig. 8. There is good overall agreement for Ar through Ni, but the observed abundances of Si and S are not well reproduced.

While the observed abundance pattern in W49B does not favor an hypernova explosion of sufficient energy to generate a GRB, we cannot definitely exclude that W49B was related to such an event.

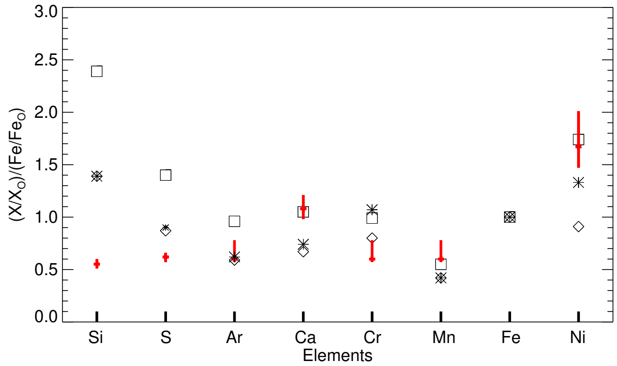

Figure 8. Elemental abundances in the central X-ray barrel of W49B (red crosses, see Table 4), normalized to the Fe abundance relative to the solar values (Anders & Grevesse 1989), compared with the yields obtained from the aspherical explosion models 25a (boxes) and 25b (diamonds) and from the spherical model 25Sa (stars) of explosive nucleosynthesis by Maeda & Nomoto (2003). The Cr and Mn abundances in the central barrel have been derived from the Ar abundance following Hwang et al. (2000).

5. Summary and conclusions

Our study of the *XMM-Newton* observations of the Galactic supernova remnant W49B has shown that:

- The remnant presents a complex X-ray morphology characterized by centrally barrel-shaped emission (*b*), terminated on the eastern side by an elongated perpendicular structure (*a*) and on the western side by a more diffuse, nearly aligned structure (*c*).
- The physical conditions of the plasma are not homogeneous throughout the remnant. Lower temperatures are found in remnant's western end, while hotter regions are located in the center and northeast.
- A high Ni overabundance ($Ni/Ni_\odot = 10^{+2}_{-1}$) has been measured in the central barrel, and the presence of Cr and Mn lines in the global spectrum is confirmed.
- We found no evidence for overionization of the plasma in the center of W49B.
- The X-ray emission from all the observed regions of W49B originates in the ejecta, based on significant element overabundances of Si, S, Ar, Ca and Fe. The equivalent width maps of W49B and a detailed spectral analysis of individual regions both show that the central (*b*) and eastern (*a*) structures have similar abundances, and the western (*c*) region exhibits lower abundances. This decrease is particularly pronounced for iron.
- The X-ray morphology of W49B may be attributed to preexisting structures in the ambient medium which may have produced an aspherical reverse shock, or alternatively to an aspherical supernova explosion in a wind cavity (bounded by molecular clouds on the eastern side of the remnant). Because it has abundances similar to those in the central barrel, the eastern structure *a* can be considered as the head of the jet. It is distorted and deviates mostly southward due to its impact with the dense molecular wall that confines its expansion to the east.
- We investigated the possibility that W49B is a γ-ray burst remnant by comparing the observed abundances with yields derived from supernova and hypernova nucleosynthesis models. We found better agreement with the less energetic ($E \sim 10^{51}$ erg) models. The association of W49B with a GRB is therefore not necessarily implied by the spectral data.

Acknowledgements. We thank the referee, Dr B. Aschenbach, for his comments and suggestions. The authors wish to thank Joseph Lazio for providing us with the 327 MHz radio image of W49B. M. M. thanks Costanza Argiroffi for the discussions about the ionization temperature. This work was partially supported by the Ministère français des Affaires Etrangères.

References

Anders, E. & Grevesse, N. 1989, Geochim. Cosmochim. Acta, 53, 197

Arnaud, K. A. 1996, in ASP Conf. Ser. 101: Astronomical Data Analysis Software and Systems V, 17
Arnaud, M., Neumann, D. M., Aghanim, N., et al. 2001, A&A, 365, L80
Bleeker, J. A. M., Willingale, R., van der Heyden, K., et al. 2001, A&A, 365, L225
Bocchino, F., Maggio, A., & Sciortino, S. 1999, A&A, 342, 839
Fujimoto, R., Tanaka, Y., Inoue, H., et al. 1995, PASJ, 47, L31
Galama, T. J., Vreeswijk, P. M., van Paradijs, J., et al. 1998, Nature, 395, 670
Hwang, U., Petre, R., & Hughes, J. P. 2000, ApJ, 532, 970
Iwamoto, K., Mazzali, P. A., Nomoto, K., et al. 1998, Nature, 395, 672
Kawasaki, M., Ozaki, M., Nagase, F., Inoue, H., & Petre, R. 2005, ApJ, 631, 935
Keohane, J. W., Reach, W. T., Rho, J., & Jarrett, T. H. 2004, American Astronomical Society Meeting Abstracts, 204,
Khokhlov, A. M., Höflich, P. A., Oran, E. S., et al. 1999, ApJ, 524, L107
Lacey, C. K., Lazio, T. J. W., Kassim, N. E., et al. 2001, ApJ, 559, 954
Lampton, M., Margon, B., & Bowyer, S. 1976, ApJ, 208, 177
Liedahl, D. A., Osterheld, A. L., & Goldstein, W. H. 1995, ApJ, 438, L115
MacFadyen, A. I. & Woosley, S. E. 1999, ApJ, 524, 262
Maeda, K. & Nomoto, K. 2003, ApJ, 598, 1163
Mazzali, P. A., Nomoto, K., Patat, F., & Maeda, K. 2001, ApJ, 559, 1047
Mewe, R., Gronenschild, E. H. B. M., & van den Oord, G. H. J. 1985, A&AS, 62, 197
Mewe, R., Lemen, J. R., & van den Oord, G. H. J. 1986, A&AS, 65, 511
Moffett, D. A. & Reynolds, S. P. 1994, ApJ, 437, 705
Nomoto, K., Maeda, K., Umeda, H., et al. 2003, in A Massive Star Odissey, from Main Sequence to Supernova, ed. K. A. van der Hucht, A. Herrero, C. Esteban (ASP), Proc. IAU Symp. 212, 395
Park, S., Hughes, J. P., Slane, P. O., et al. 2004, ApJ, 602, L33
Pye, J. P., Thomas, N., Becker, R. H., & Seward, F. D. 1984, MNRAS, 207, 649
Radhakrishnan, V., Goss, W. M., Murray, J. D., & Brooks, J. W. 1972, ApJS, 24, 49
Read, A. M. & Ponman, T. J. 2003, A&A, 409, 395
Rho, J. & Petre, R. 1998, ApJ, 503, L167
Smith, A., Peacock, A., Jones, L. R., & Pye, J. P. 1985, ApJ, 296, 469
Strüder, L., Briel, U., Dennerl, K., et al. 2001, A&A, 365, L18
Turner, M. J. L., Abbey, A., Arnaud, M., et al. 2001, A&A, 365, L27
Willingale, R., Bleeker, J. A. M., van der Heyden, K. J., Kaastra, J. S., & Vink, J. 2002, A&A, 381, 1039